Journal of the Chinese Society of Mechanical Engineers, Vol.47, No.3, pp 251~262 (2026)

A Thermal Elastoplastic Fractal Surface Contact Modelling Approach and Its Application in Combined Rotors

Ya-Zheng Zhao*, Jin Zhou**, Yang Zhou*, Yong-Hui Wang*** and Yuan-Ping Xu****

Keywords：thermal elastoplastic, contact stiffness, combined rotor, fractal model.

ABSTRACT

A thermal elastoplastic fractal contact stiffness model is presented to investigate the impact of temperature on interface stiffness characteristics and combined rotor vibration. The normal total load and contact stiffness of the asperities and the bolt are derived under temperature conditions, using fractal geometry theory. A thermal elastoplastic rotor dynamic model, which considers surface contact, is proposed by utilizing the Lagrange equation and the equivalent spring energy change between the contact interfaces. Numerical analysis demonstrates that the contact stiffness exhibits nonlinearity with the increase of temperature difference, resulting in a significant increase in the total normal stiffness. Additionally, the impact of interface thermal stiffness on the rotor dynamic characteristics of each order is different.

INTRODUCTION

The interface contact model is crucial for ensuring accurate modelling of assembled rotors with numerous connecting interfaces, such as aero-engines and gas turbines. This model significantly impacts the accuracy of dynamic characteristics analysis. In contrast to rotors operating at room temperature, turbine rotors operate under prolonged exposures to high temperatures. The temperature field induces nonlinearity in the connection stiffness, subsequently influencing the dynamic characteristics of the combined rotor. Accordingly, the establishment of a thermal elastoplastic coupling interface contact model holds great engineering importance for accurately calculating dynamic characteristics and controlling vibration in combined rotors operating under high temperature conditions.

Extensive research has been conducted on interface contact modelling and characteristic analysis, predominantly emphasizing the characteristics neglecting the influence of temperature conditions. Li et al. (Li et al., 2021) proposed an improved Iwan contact model that considers the distribution characteristics of interface contact pressure. They explored the influence of different pressure distributions on the hysteresis characteristics. Li et al. (Li et al., 2019) presented a Coulomb friction contact model derived from the Iwan model and conducted a comprehensive analysis of the impact of contact pressure distribution on this proposed model. Liu et al. (Liu et al., 2019a) introduced an analytical model for determining the interface contact stiffness between the toolholder and spindle the. The analysis results demonstrate that temperature can induce variations in both the dimensionless contact area and contact stiffness. Shi et al. (Shi and Zhang, 2022) established a fractal model to characterize contact parameters and investigated the influence of bolt preload, friction coefficient and contact load ratio on contact characteristics. Yin et al. (Yin et al., 2018) proposed a modified three-dimensional fractal normal contact stiffness model. Zhou et al. (Zhou et al., 2022) described an equivalent normal stiffness for bolted joints. The effects of external force, fractal parameters and preload on contact stiffness were explored. Ping et al. (Ping et al., 2018) examined the influence of non-parallel factors of bolt contact surface on the contact stiffness and rotor dynamic characteristics. Peng et al.

Paper Received April, 2024. Revised May, 2025. Accepted June, 2025. Author for Correspondence:Jin Zhou.

* *Doctorate student, College of Mechanical and Electrical Engineering, Nanjing University of Aeronautics and Astronautics, Nanjing 210016, China*

** *Professor, College of Mechanical and Electrical Engineering, Nanjing University of Aeronautics and Astronautics, Nanjing 210016, China*

*** *Graduate Student, College of Mechanical and Electrical Engineering, Nanjing University of Aeronautics and Astronautics, Nanjing 210016, China*

**** *Associate Professor, College of Mechanical and Electrical Engineering, Nanjing University of Aeronautics and Astronautics, Nanjing 210016, China*

(Peng et al., 2013) developed a finite element model of asperity contact to investigate the impact of surface morphology and material properties on the contact characteristics. Hou et al. (Hou and Zhang, 2022) utilized a finite element model of the bolted connection structure to analyze the influence of the thickness of connector thickness, nut diameter, and the empirical formula for connection stiffness on contact stress. Zhao et al. (Zhao et al., 2018) characterized the interface contact stiffness with a thin layer element, and investigated the regularity of the bolt preload on the stiffness. Shamot et al. (Shamoto et al., 2014) developed an analytical method for predicting the contact stiffness and discussed the nonlinear stiffness under various preload forces. Xiao et al. (Weiwei Xiao et al., 2014) represented the contact stiffness of bolts as the stiffness matrix of the finite element model. Hartwigsen et al. (Hartwigsen et al., 2004) designed an experimental method to investigate the impact of bolt connections on structural dynamics.

Analytical method, numerical method and experiment are performed to the study of interface contact rough surface. These research works mainly focus on the influence of bolt preload, roughness, material properties and other parameters on the contact characteristics of the interface, ignoring the influence of temperature on the interface characteristics of bolted joints. Currently, most of the research objects on the influence of temperature are cylindrical surfaces. Limited research exists on the fractal model of bolt connections under temperature.

The majority of research pertaining to the combined rotor in a temperature field concentrates on examining the influence of temperature on the interface stress distribution, as well as the influence of interface characteristics on the contact thermal conductivity. Yuan et al. (Yuan et al., 2010) developed a finite element model for the heavy duty gas turbine. The paper analyzed the changes in contact stress of curvic couplings under a temperature field. Zheng et al. (Si et al., 2020) utilized the finite element model of contact friction element to analyze the temperature field and temperature stress. Cheng et al. (Cheng et al., 2020) presented a finite element model of tool joint considering thermal mechanical coupling, and examined the variations in temperature field, contact stress and working torque of contact surface. They found that the limit torque decreases under the temperature field. This phenomenon is commonly referred to as temperature induced bolt stress relaxation in the interface of a bolted joint. Magyar et al. (Magyar and Sauer, 2017) established a stress field for the interface under temperature conditions based on fractal geometry. The research revealed that the increase of interface temperature results in elevated interface contact stress. Majumdar (Majumdar and Tien, 1991) introduced a novel model that utilizes the fractal characterization of surface roughness to analyze thermal contact conductance between two rough contact surfaces. Subsequently, multiple scholars (Liu et al., 2019b; Tirovic and Voller, 2005) have further developed the interface contact thermal conductance model on this basis. Sun et al. (Sun and Xing, 2023) proposed a fractal model of rough surface contact thermal conductivity, taking into account elliptical asperities. Ajul et al. (Ajul and Chanda, 2023) investigated the impact of varying bolt torques on the interfacial contact thermal conductance.

In addition, for the combined rotor, there are numerous textbooks and articles dedicated to analyze the influence of temperature on the dynamic characteristics of the whole rotor. Ziaei-Rad et al. (Ziaei-Rad et al., 2010) derived the equivalent bending moment equation into the rotor kinematics equation, and subsequently examined the influence of temperature on the dynamic characteristics. Peng et al. (Peng et al., 2020) conducted an investigation on the thermal bending phenomenon arising from natural convection. They performed experiments to analyze the effects of deformation and eccentricity, which yielded valuable input data for the determination of the equivalent thermal bending moment in rotor dynamics.

The literature review reveals that the research on the vibration characteristics of the thermal elastoplastic coupling in combined rotor mainly has the following two limitations. Firstly, the influence of temperature on the contact characteristics of bolted joints is rarely explored. Secondly, the modelling and vibration characteristics analysis of thermal elastoplastic coupled combined rotors often neglect the interface thermal stiffness. Therefore, the present study proposes a thermal elastoplastic fractal surface contact stiffness model, based on fractal theory. This model is used for modelling a combined rotor system, aiming to accurately describe the dynamic characteristics of thermal elastoplastic coupling in the rotor. Moreover, the characteristics of contact stiffness under temperature field are analyzed and the essential reason of stiffness change is analyzed. Finally, the influence of interface thermal stiffness on the dynamic characteristics of the thermal elastoplastic coupling combined rotor is discussed.

THERMAL ELASTOPLASTIC COUPLING CONTACT ANALYTICAL MODEL

This section introduces a contact model for the asperity interface that considers temperature load, utilizing fractal theory. Then the contact stiffness model of thermal elastoplastic coupling bolt which can be directly used in finite element model is determined by the relationship between interface stiffness and load distribution. Finally, the dynamic model of thermal elastoplastic coupled combined rotor considering thermal elastoplastic fractal surface contact is derived.

Thermal elastoplastic coupling asperity contact model

As depicted in Figure 1, the micro-contact between rough surface-a and surface-b can be simplified as the interaction between a rigid plane and a rough surface. The asperity is in different deformation regions under different contact areas.

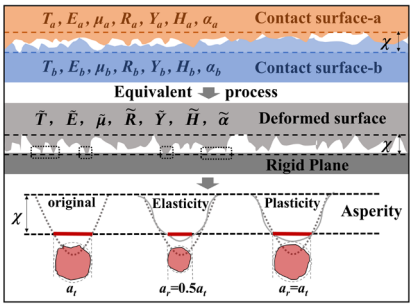

Fig. 1 Micro-contact schematic diagram

The contact thermal conductance causes a difference between the temperatures T_a and T_b of the two contact surfaces, and the equivalent temperature is $\tilde{T} = (T_a R_b + T_b R_a)/(R_a + R_b)$ (Shlykov et al., 1964). The elastic modulus of the two contact surfaces are E_a and E_b, the Poisson 's ratio are μ_a and μ_b, the asperity radius are R_a and R_b, the yield strength are Y_a and Y_b, the material hardness are H_a and H_b, and the thermal expansion coefficient are α_a and α_b. The equivalent asperity radius $\tilde{R} = (R_a^{-1}+R_b^{-1})^{-1}$, the equivalent elastic modulus $\tilde{E} = [(1-\mu_a^2)/E_a + (1-\mu_b^2)/E_b]^{-1}$, the equivalent yield strength $\tilde{Y} = \min(Y_a, Y_b)$, the equivalent hardness $\tilde{H} = \min(H_a, H_b)$, and the equivalent thermal expansion coefficient $\tilde{\alpha} = (\alpha_a^{-1}+\alpha_b^{-1})^{-1}$ are defined.

Since the actual contact surface is inherently rough, it is traditionally characterized using statistical parameters such as asperity height, slope, and radius. However, such descriptions strongly depend on the resolution of the measurement equipment and the selected sampling length, limiting their universality and accuracy. To overcome these limitations, fractal geometry is introduced to characterize the rough surface. The key advantage of fractal theory is its ability to describe surface features at multiple scales — as the observation scale decreases, finer surface details continue to emerge. This scale-invariance property allows for a more realistic and comprehensive description of surface topography. Related studies have shown that the height function of the three-dimensional isotropic surface can be described by the improved Weierstrass-Mandelbrot function (Yan and Komvopoulos, 1998):

$$z(x,y) = L\left(\frac{G_f r}{L}\right)^{(D_f-1)}\left(\frac{\ln\gamma}{M}\right)^{\frac{1}{2}}\sum_{m=1}^{M}\sum_{n=0}^{n_{max}}\gamma^{(D_f-2)n}\times \left\{\cos\phi_{m,n} - \cos\left[\frac{2\pi\gamma^n(x^2+y^2)^{\frac{1}{2}}\cos\left(\tan^{-t}\left(\frac{y}{x}\right)-\frac{\pi m}{m_0}\right)}{L} + \phi_{m,n}\right]\right\}, \quad (1)$$

where $z(x,y)$ is the fractal profile of the plane xoy, L is the sample length, and $1/L$ is the sampling frequency. D_f is the fractal dimension of fractal profile, which is used to describe the density of rough surface. Fractal roughness G_f is a frequency independent height scaling parameter and γ is a parameter that determines the frequency density of fractal profile. $\phi_{m,n}$ is a random phase used to prevent the coincidence of different frequencies on the surface profile. L_s represents the truncation length, and the upper limit of the frequency index n is expressed as $n = \lceil log\,(L/L_s)/log\gamma \rceil$ when the highest frequency is equal to $1/L_s$. m_0 is used to represent the dimension of the rough surface. A two-dimensional rough surface profile ($m_0 = 1$) is represented as in Equation (2).

$$z(x) = (ln\gamma)^{\frac{1}{2}}{G_f}^{D_f-1}L^{2-D_f}\sum_{n=0}^{n_{max}}\gamma^{(D_f-2)n} \times\left[\cos\phi_{1,n} - \cos\left(\frac{2\pi\gamma^n x}{L}-\phi_{1,n}\right)\right], \quad (2)$$

where x is the transverse coordinate of the asperity, and $z(x)$ is the longitudinal coordinate (the height direction of the rough surface). For an asperity with a truncation radius of r_t, the truncation length L_s is $2r_t$, and then the frequency index is expressed as $n_t = int[log\,(L/2r_t)/log\gamma]$. The surface profile function $z_t(x)$ of the asperity with truncation radius r_t can be obtained:

$$z_t(x) = 2^{2-D_f}(ln\gamma)^{\frac{1}{2}}{r_t}^{2-D_f}{G_f}^{D_f-1} \times\left[\cos\phi_{1,n_t} - \cos\left(\frac{\pi x}{r_t}-\phi_{1,n_t}\right)\right]. \quad (3)$$

When $\phi_{1,n_t} = 0$ and $x = r_t$, satisfying $\left[\cos\phi_{1,n_t} - \cos(\pi x/r_t - \phi_{1,n_t})\right]_{max} = 2$, the maximum z_t is the deformation χ of the asperity in the z direction.

$$\chi = 2^{3-D_f}(ln\gamma)^{\frac{1}{2}}{r_t}^{2-D_f}{G_f}^{D_f-1} = 2^{3-D_f}\pi^{\frac{(D_f-2)}{2}}(ln\gamma)^{\frac{1}{2}}{G_f}^{D_f-1}{a_t}^{\frac{(2-D_f)}{2}}. \quad (4)$$

$\chi = \chi_c$ is the critical point of the elastic and plastic deformation region. The truncated asperity satisfies the relationship ${r_t}^2 + \chi^2 - 2\tilde{R}\chi = 0$. Since $\chi \ll \tilde{R}$, the truncation radius is expressed as $r_t =$

$\left(2\tilde{R}\chi\right)^{1/2}$, and the equivalent radius of the asperity is obtained by substituting Equation (4) into the geometric relationship:

$$\tilde{R} = {r_t}^{D_f} 2^{D_f-4} (ln\gamma)^{-\frac{1}{2}} {G_f}^{D_f-1} = 2^{D_f-4} \pi^{-\frac{D_f}{2}} (ln\gamma)^{-\frac{1}{2}} {G_f}^{D_f-1} {a_t}^{\frac{D_f}{2}}. \quad (5)$$

The contact load of asperity is mainly composed of mechanical load and temperature load. For the isotropic material structure, the normal strain in each direction is the same ($\varepsilon = \tilde{\alpha}\Delta\tilde{T}$) and there is no shear strain ($\tau = 0$). When $\chi \le \chi_c$, the asperity undergoes elastic deformation. Based on the Hertz contact theory and thermal strain expression, the following relationships are obtained as below (Kogut and Komvopoulos, 2004):

$$f_{e_M} = \frac{2^{\frac{3}{2}}}{3}\tilde{E}\chi r_t = \frac{2^{4.5-D_f}}{3}\pi^{\frac{(D_f-3)}{2}}(ln\gamma)^{\frac{1}{2}}\tilde{E}{G_f}^{D_f-1}{a_t}^{\frac{(3-D_f)}{2}}, \quad (6)$$

$$f_{e_T} = \tilde{\alpha}\Delta\tilde{T}\tilde{E}a_r = \frac{1}{2}\tilde{\alpha}\Delta\tilde{T}\tilde{E}a_t, \quad (7)$$

$$a_r = \frac{1}{2}a_t, \quad (8)$$

where f_{e_M} and f_{e_T} are normal preload and temperature load, respectively. The real contact area is $a_r = \pi r_r^2$, and the truncated contact area is $a_t = \pi r_t^2$. When $\chi > \chi_c$, the asperity is in the plastic deformation zone, which satisfies the following relationships:

$$f_{p_M} = \tilde{H}a_r = \tilde{H}a_t, \quad (9)$$

$$f_{p_T} = \tilde{\alpha}\Delta\tilde{T}\tilde{E}a_r = \tilde{\alpha}\Delta\tilde{T}\tilde{E}a_t, \quad (10)$$

$$a_r = a_t. \quad (11)$$

The total normal loads of the asperity in the elastic and plastic deformation regions are stated as:

$$f_e = f_{e_M} + f_{e_T}, \quad (12)$$

$$f_p = f_{p_M} + f_{p_T}. \quad (13)$$

Substituting Equations (6)-(11) into (12) and (13), the total normal loads of the asperity are obtained as below:

$$f_e(a_t) = \frac{2^{4.5-D_f}}{3}\pi^{\frac{(D_f-3)}{2}}\tilde{E}(ln\gamma)^{\frac{1}{2}} \times {G_f}^{D_f-1}{a_t}^{\frac{(3-D_f)}{2}} + \frac{1}{2}\tilde{\alpha}\Delta\tilde{T}\tilde{E}a_t, \quad (14)$$

$$f_p(a_t) = \tilde{H}a_t + \tilde{\alpha}\Delta\tilde{T}\tilde{E}a_t. \quad (15)$$

By substituting the critical deformation into the deformation Eq. (4), the critical truncation area a_{t_c} can be expressed as (Tian, 2013) follows:

$$a_{t\_c} = 2{G_f}^2\left(\frac{\tilde{H}}{2\tilde{E}}\right)^{\frac{2}{1-D_f}}. \quad (16)$$

The distribution function of the asperity with truncated area a_t is described as Equation (17).

$$n(a_t) = \frac{1}{2}D_f\varphi^{\frac{2-D_f}{2}}a_{t\_max}^{\frac{D_f}{2}}a_t^{-\frac{D_f+2}{2}}, a_t \in [0, a_{t\_max}], \quad (17)$$

where a_{t_max} represents the maximum truncation area of the asperity, and the domain expansion factor φ satisfies the following relation:

$$\varphi^{\frac{2-D_f}{2}} - \left(1+\varphi^{-\frac{1}{2D_f}}\right)^{1-\frac{2}{D_f}} - \frac{2}{D_f} + 1 = 0, D_f \in (1,2). \quad (18)$$

When the surface asperities are evenly distributed, the total truncated contact area A_t can be defined as:

$$A_t = \int_0^{a_{t\_max}} a_t\, n(a_t) da_t. \quad (19)$$

The total actual contact area A_r is $0.5A_t$. Substituting Eq. (17) into Equation (19), the maximum truncation area of the asperity is described as:

$$a_{t\_max} = A_t {D_f}^{-1}(2-D_f)\varphi^{\frac{D_f-2}{2}}. \quad (20)$$

For a contact area of A_r, the total normal load of the bolt can be expressed by the integral of the normal load and the distribution density of the asperity:

$$\begin{aligned} F &= \int_{a_{t_c}}^{a_{t\_max}} f_e(a_t)n(a_t)da_t + \int_0^{a_{t_c}} f_p(a_t)n(a_t)da_t \\ &= \frac{2^{4.5-D_f}D_f\pi^{\frac{D_f-3}{2}}}{3(3-2D_f)}\tilde{E}(ln\gamma)^{\frac{1}{2}}{G_f}^{D_f-1}\varphi^{\frac{2-D_f}{2}}a_{t\_max}^{\frac{D_f}{2}} \times\left[a_{t\_max}^{\frac{3-D_f}{2}} - a_{t\_c}^{\frac{3-D_f}{2}}\right] \\ &+ \frac{D_f}{2(2-D_f)}\tilde{\alpha}\Delta\tilde{T}\tilde{E}\varphi^{\frac{2-D_f}{2}}a_{t\_max}^{\frac{D_f}{2}}\left[a_{t\_max}^{(2-D_f)/2} - a_{t\_c}^{(2-D_f)/2}\right] \\ &+ \left[\frac{D_f}{2-D_f}\tilde{H}\varphi^{\frac{2-D_f}{2}} + \frac{D_f}{2-D_f}\tilde{\alpha}\Delta\tilde{T}\tilde{E}\varphi^{\frac{2-D_f}{2}}\right] \times a_{t\_max}^{\frac{D_f}{2}}a_{t\_c}^{(2-D_f)/2}. \end{aligned} \quad (21)$$

The temperature load F_T and the preload F_M are written as:

$$F_T = \frac{D_f}{2(2-D_f)}\tilde{\alpha}\Delta\tilde{T}\tilde{E}\varphi^{\frac{2-D_f}{2}}a_{t\_max}^{\frac{D_f}{2}} \times\left[a_{t\_max}^{(2-D_f)/2} + a_{t_c}^{(2-D_f)/2}\right], \quad (22)$$

$$F_M = \frac{2^{4.5-D_f}\pi^{\frac{D_f-3}{2}}}{3(3-2D_f)}\tilde{E}(ln\gamma)^{\frac{1}{2}}{G_f}^{D_f-1}\varphi^{\frac{2-D_f}{2}}a_{t\_max}^{\frac{D_f}{2}} \times\left[a_{t\_max}^{\frac{3-D_f}{2}} - a_{t\_c}^{\frac{3-D_f}{2}}\right] + \frac{D_f}{2-D_f}\tilde{H}\varphi^{\frac{2-D_f}{2}}a_{t\_max}^{\frac{D_f}{2}}a_{t\_c}^{(2-D_f)/2}. \quad (23)$$

The above expression applies to $D_f \in (1,2)$and

$D_f \neq 1.5$. When D_f=1.5, the Equation (23) becomes undefined due to a zero denominator. To address this issue, D_f=1.5 is instead substituted into Eqs. (14), (15), and (17). Accordingly, the total normal load of the bolt under this condition is expressed as follows:

$$F = \frac{3}{2}\tilde{\alpha}\Delta\tilde{T}\tilde{E}\varphi^{\frac{1}{4}}a_{t\_max}^{\frac{3}{4}}\left[a_{t\_max}^{\frac{1}{4}} + a_{t\_c}^{\frac{1}{4}}\right] + \frac{2}{\pi^{\frac{3}{4}}}\tilde{E}(ln\gamma)^{\frac{1}{2}}G_f^{\frac{1}{2}}\varphi^{\frac{1}{4}}a_{t\_max}^{\frac{3}{4}}ln\left(\frac{a_{t\_max}}{a_{t_c}}\right) + 3\varphi^{\frac{1}{4}}\tilde{H}a_{t\_max}^{\frac{3}{4}}a_{t\_c}^{\frac{1}{4}}. \quad (24)$$

Contact stiffness of thermal elastoplastic coupling bolt

The bolt contact stiffness is considered as the parallel stiffness of each asperity in the contact surface, which can be determined by the integral of the asperity stiffness k_n and the distribution function $n(a_t)$. The normal contact stiffness of the asperity is defined as follows:

$$k_n = \frac{df_e(a_t)}{d\chi(a_t)} = \frac{df_e(a_t)/da_t}{d\chi(a_t)/da_t}. \quad (25)$$

Substituting the normal load and deformation of the asperity into the above formula, two relationships are obtained:

$$\begin{cases} \dfrac{df_e(a_t)}{da_t} = \dfrac{3-D_f}{3}2^{\left(\frac{7}{2}-D_f\right)}\pi^{\frac{D_f-3}{2}} \times \tilde{E}(ln\gamma)^{\frac{1}{2}}G_f{}^{D_f-1}a_t^{\frac{1-D}{2}} + \dfrac{1}{2}\tilde{\alpha}\Delta\tilde{T}\tilde{E} \\ \dfrac{d\chi(a_t)}{da_t} = (2-D_f)2^{2-D_f}\pi^{\frac{D_f-2}{2}} \times (ln\ \gamma)^{\frac{1}{2}}G_f{}^{D_f-1}a_t^{-\frac{D_f}{2}} \end{cases}. \quad (26)$$

Substituting the above formulas into Equation (25), the normal contact stiffness of the asperity is indicated as:

$$k_n = \frac{2^{\frac{3}{2}}(3-D_f)\pi^{-\frac{1}{2}}}{3(2-D_f)}\tilde{E}a_t^{\frac{1}{2}} + \frac{2^{D_f-3}}{2-D_f}\pi^{\frac{2-D_f}{2}}\tilde{\alpha}\Delta\tilde{T}\tilde{E}(ln\gamma)^{\frac{1}{2}}G_f{}^{1-D_f}a_t^{\frac{D_f}{3}}. \quad (27)$$

Therefore, the normal contact stiffness of a bolted connection can be expressed as follows:

$$K_n = \int_{a_{t_c}}^{a_{t\_max}} k_n n(a_t)da_t = \frac{2^{\frac{3}{2}}(3-D_f)D_f\pi^{-\frac{1}{2}}}{3(2-D_f)(1-D_f)}\tilde{E}\varphi^{\frac{2-D_f}{2}}a_{t\_max}^{\frac{D_f}{2}}\left[a_{t\_max}^{\frac{1-D_f}{2}} - a_{t_c}^{\frac{1-D_f}{2}}\right] + \frac{2^{D-4}D\pi^{\frac{2-D_f}{2}}}{2-D}\tilde{\alpha}\Delta\tilde{T}\tilde{E}(ln\gamma)^{-\frac{1}{2}} \times G_f{}^{1-D_f}\varphi^{\frac{2-D_f}{2}}a_{t\_max}^{\frac{D_f}{2}}ln\left(\frac{a_{t\_max}}{a_{t\_c}}\right). \quad (28)$$

The normal contact stiffness K_n of the bolt is composed of the mechanical contact stiffness K_{n_M} and the temperature contact stiffness K_{n_T}.

Thermal elastoplastic coupling combined rotor model

The contact interface is described as the massless spring element with the normal stiffness k_f and the tangential stiffness k_q. Based on the Lagrange equation, the additional contact stiffness matrix K_c is obtained as follows (Han et al., 2021):

$$K_c = \begin{bmatrix} diag(a,a,b,b) & diag(-a,-a,-b,-b) \\ diag(-a,-a,-b,-b) & diag(a,a,b,b) \end{bmatrix}, \quad (29)$$

where $a = 0.5k_q\pi r^2$, $b = 0.125k_f\pi r^4$, and r is the radius of the contact surface. k_f and k_q are expressed as:

$$\begin{cases} k_f = \dfrac{\sum_i^N K_{ni}}{\pi r^2}, \\ k_q = \beta k_f \end{cases} \quad (30)$$

where N is the number of bolts, K_{ni} is the normal contact stiffness of the i-th bolt, and β is the proportional coefficient of tangential stiffness and normal stiffness. Based on the finite element method, the motion equation of the thermal elastoplastic coupling combined rotor is as follows:

$$M\ddot{q} + [C + \Omega G]\dot{q} + \left(K + K_T + K_c + K_{spring}\right)q = 0, \quad (31)$$

where matrix $M, C, G, K, K_T, K_c, K_{spring}$ are the mass, damping, gyroscopic, stiffness, temperature load dominated stiffness, contact thermal stiffness and bearing support stiffness matrix of the thermal elastoplastic coupling rotor system. $q, \dot{q}$ and $\ddot{q}$ are generalized coordinates and its first derivative and second derivative respectively. Contact thermal stiffness K_c explicitly defines the relationship between force and displacement at contact interfaces under thermal loads. In the assembly of the model, contact thermal stiffness directly alters the rotor's stiffness matrix, thereby influencing natural frequencies, critical speeds, and vibration amplitudes.

NUMERICAL SIMULATION AND MODEL VALIDATION

Figure 2 depicts the solution process of the interface contact thermal stiffness characteristics and the dynamic characteristics of the thermal elastoplastic coupling combined rotor model based on the model proposed in the previous section.

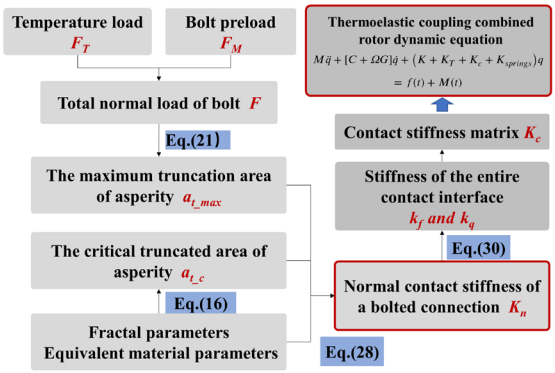

Fig. 2 Solution procedure

Analysis of contact thermal stiffness characteristics

In this section, the contact thermal stress of the combined rotor under different steady state temperature fields is analyzed by the finite element method, and the temperature load F_T is solved based on the average thermal stress. The mathematical expression of preload F_M is given by analyzing the contact pressure distribution of single bolt connection. Figure 3 illustrates the distribution of contact thermal stress at varying temperature fields. The results show that the thermal pressure along the contact interface is non-uniform and decreases gradually from the center outward. Moreover, it can be observed that the overall magnitude of the contact pressure increases with the temperature difference.

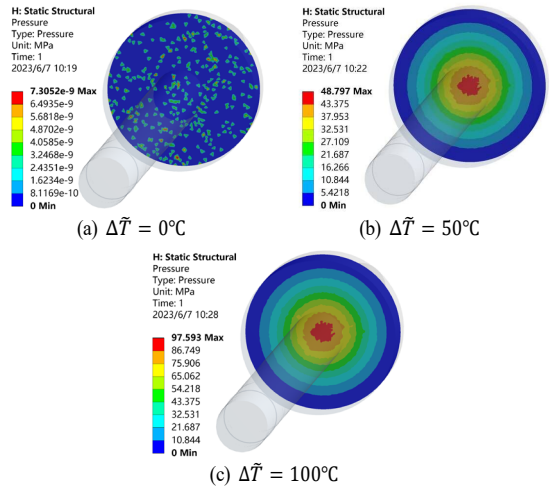

(a) $\Delta\tilde{T}$ = 0℃ (b) $\Delta\tilde{T}$ = 50℃

(c) $\Delta\tilde{T}$ = 100℃

Fig. 3 Distribution of contact thermal pressure

The average thermal pressure $\overline{p_T}$ of the contact surface is extracted using post-processing functions, and its linear relationship with the temperature difference $\Delta\tilde{T}$ is established as:

$$\overline{p_T} = 2.8717 \times 10^5 \cdot \Delta\tilde{T}, \Delta\tilde{T} \in [0,200]℃. \quad (32)$$

The bolt interface contact temperature load F_T is defined as follows:

$$F_T = \iint \overline{p_T} dA_r = 2.8717 \times 10^5 \cdot A_r \cdot \Delta\tilde{T}, \Delta\tilde{T} \in [0,200]℃. \quad (33)$$

The relationship between the preload moment M_b and the bolt preload force F_b is approximately expressed as:

$$F_b = \frac{5M_b}{d}, \quad (34)$$

where d=8mm is the nominal bolt diameter. For a tightening torque of 8 Nm, the preload force is $F_M = F_b$=5kN. Therefore, the total normal load F of a bolt is expressed as:

$$F = F_T + F_M = 2.8717 \times 10^5 \cdot A_r \cdot \Delta\tilde{T} + \frac{5M_b}{d}. \quad (35)$$

The above formula applies to $\Delta\tilde{T} \in [0,200]℃$. The total normal load F is employed as an input to the solution procedure shown in Fig. 2, through which the contact thermal stiffness matrix K_c is derived and subsequently integrated into the rotor dynamic model Equation (31).

As shown in Figure 4, the nominal contact area A_a of the single bolted joint interface is described as:

$$A_a = \pi r_m^2 - \pi\left(\frac{\alpha d}{2}\right)^2, \quad (36)$$

where the diameter factor of the bolt hole is α=1.125, and the distance from the center of the bolt hole to the boundary of the stress field is r_m=14mm.

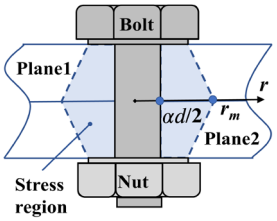

Fig. 4 Nominal contact area of bolt connection

Figure 5 shows the normal contact stiffness when the temperature difference $\Delta\tilde{T}$ of the bolt contact interface changes from 0℃ to 200℃. The stiffness dominated by temperature load in temperature field increases with the increase of temperature difference, and the growth rate increases gradually. The stiffness dominated by bolt preload increases with the increase of temperature difference, and the change rate decreases gradually. The total normal stiffness obtained by the superposition of temperature dominant stiffness and bolt preload dominant stiffness shows a nearly linear stiffness growth with the change of temperature difference.

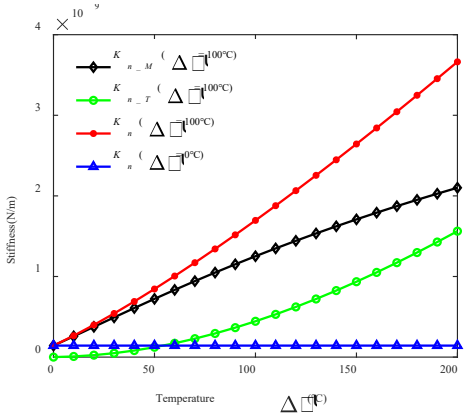

Fig. 5 Contact stiffness under different temperature conditions (D_f=1.39,$G_f = 6.37 \times 10^{-10}$)

The influence of temperature variation on the actual contact area is illustrated in Figure 6. The temperature load causes the deformation of the asperity, resulting in a change in the actual contact area, which also changes the stiffness dominated by the bolt preload and the total normal stiffness.

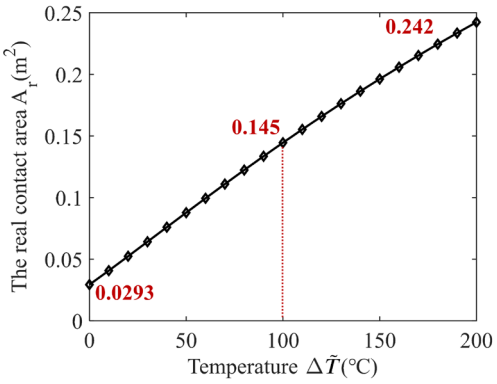

Fig. 6 Real contact area under different temperature conditions (D_f=1.39,$G_f = 6.37 \times 10^{-10}$)

Fractal dimension D_f and fractal roughness G_f are uncertain parameters in the contact stiffness model, which are usually determined by experiments (Zhou, 2025). The fractal dimension D_f characterizes the complexity of surface morphology, with higher values reflecting a denser distribution of asperities. The fractal roughness G_f defines the amplitude of surface features, such that increasing G_f yields taller asperities and more pronounced surface relief. These two parameters govern the contact stiffness in thermo-elastoplastic coupled interactions. However, variations in material properties, processing techniques, and machining precision introduce uncertainties into these two categories of parameters. To assess the impact of such uncertainties on the results, the change of bolt connection stiffness at room temperature and high temperature with the change of uncertain parameters is discussed based on the derived Equation (28). Figure 7 displays the analysis result of the interface contact stiffness under different temperature conditions when G_f changes from 10^{-12} to 10^{-10}. Note that the contact stiffness decreases with the increase of G_f at high temperature and room temperature. When D_f changes from 1.35 to 1.45, interface contact stiffness is shown in Figure 8. The results indicate that the contact stiffness remains relatively stable when G_f and D_f vary within the ranges of [2×10^{-11}, 1×10^{-10}] and [1.35~1.4], respectively. However, when $G_f < 2\times10^{-11}$ or $D_f > 1.4$, the contact stiffness exhibits high sensitivity to these parameters.

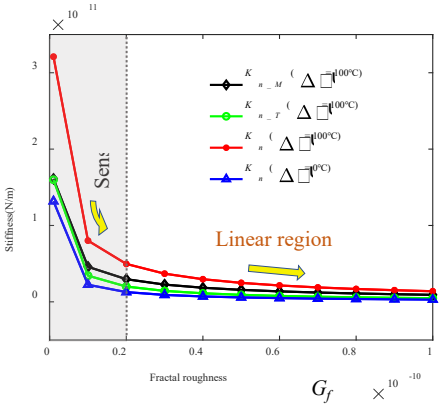

Fig. 7 Contact stiffness under different fractal roughness G_f (D_f=1.39)

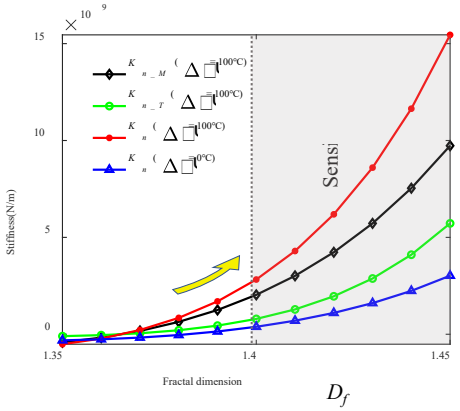

Fig. 8 Contact stiffness under different fractal dimension D_f ($G_f = 6.37 \times 10^{-10}$)

Dynamic characteristics analysis of thermal elastoplastic coupling combined rotor

As shown in Figure 9, the combined rotor with speed of Ω is connected by six circumferentially distributed bolts. The rotor is supported by two bearings. Detailed parameters are listed in Table 1.

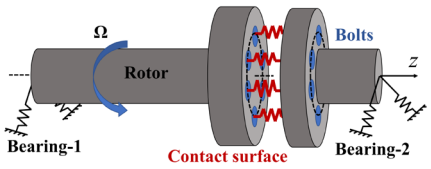

Fig. 9 Schematic diagram of combined rotor with bolt connection

Table 1 Parameters of the combined rotor system

Parameter	Value
Elastic modulus E_a, E_b	2.05×10^{11} Pa
Poisson 's ratio μ_a, μ_b	0.3
Yield strength Y_a, Y_b	3.5×10^{8} Pa
Material hardness H_a, H_b	9.8×10^{8} Pa
Thermal expansion coefficient α_a, α_b	1.28×10^{-5} ℃$^{-1}$
Bolt number N	6
Support stiffness k_1, k_2	1×10^{7} N·m
Fractal dimension D_f	1.39
Fractal roughness G_f	6.37×10^{-10}
Proportional coefficient β	0.7

In this work, the one-dimensional beam finite element model is established by discretizing the rotor into beam elements. The element stiffness and mass matrices are computed based on material properties and geometry, then assembled into global matrices. Then, boundary conditions and loads are applied accordingly. The model, consisting of 16 nodes and 14 beam elements, is detailed in Figure 10.

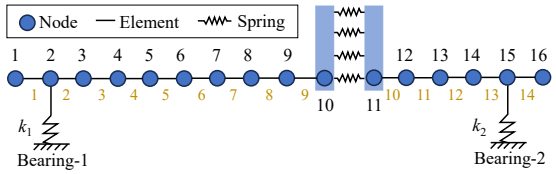

Fig. 10 Model parameters for analysis

To evaluate the accuracy of the above one-dimensional beam element model, a three-dimensional finite element model is developed for comparative analysis. In this model, the rotor is discretized using hexahedral elements, subjected to material properties and boundary conditions consistent with those of the one-dimensional model. The corresponding mesh parameters are shown in Figure 11.

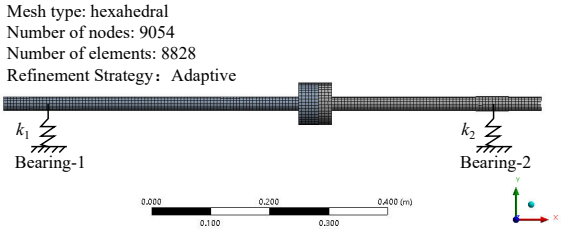

Fig. 11 Model parameters for verification

When the temperature difference $\Delta\tilde{T} = 0$℃, the natural frequency (Table 2) and mode shape (Figure 12) of the combined rotor are obtained by the two methods of beam element and SOLID45 element finite element modelling. The natural frequencies and mode shapes determined by the two methods are consistent, so that the beam model can be used to explore the vibration characteristics of the thermal elastoplastic coupling combined rotor.

Table 2 Natural frequencies obtained by two methods

Order	Beam elements NF (Hz)	ANSYS model NF (Hz)	Error (%)
1	61.82	62.689	1.40
2	61.82	63.021	1.94
3	247.40	251.56	1.68
4	247.40	252.56	2.09
5	486.55	482.34	0.86
6	486.55	482.73	0.78

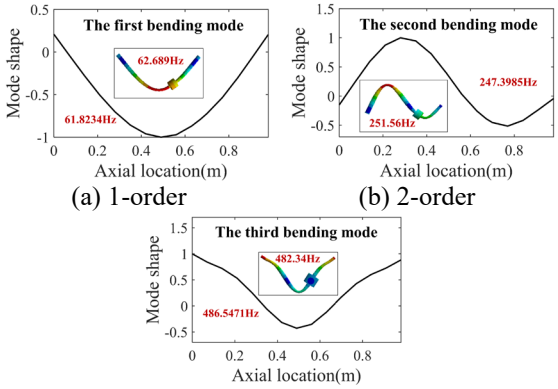

Fig. 12 The first three modal shapes by two methods

Table 3 and Table 4 show the first four natural frequencies of the temperature difference $\Delta\tilde{T}$ from 0℃ to 200℃ without considering the contact thermal stiffness and considering the contact thermal stiffness. In both cases, when the temperature difference is more than 100℃, the first-order eigenvalue disappears and the second-order eigenvalue moves forward. It is worth noting that the disappearance time of the first-order natural frequency is different in both cases.

Table 3 The natural frequencies without considering the contact thermal stiffness

$\Delta\tilde{T}$(℃)	1-order (Hz)	2-order (Hz)	3-order (Hz)	4-order (Hz)
0	61.82	247.40	486.55	556.08
50	46.83	235.91	477.31	548.49
100	17.26	222.97	467.09	540.76
150	208.28	455.52	532.90	666.76
200	191.49	442.06	524.93	642.30

Table 4 The natural frequencies considering the contact thermal stiffness

$\Delta\tilde{T}$(℃)	1-order (Hz)	2-order (Hz)	3-order (Hz)	4-order (Hz)
0	61.82	247.40	486.55	556.08
50	47.99	241.71	477.48	552.36
100	19.43	229.92	467.26	544.66
150	216.12	455.66	536.51	672.54
200	200.25	442.18	528.16	647.71

Figure 13 shows the first four natural frequencies as the temperature changes without considering the contact thermal stiffness and considering the contact thermal stiffness. As shown in Fig. 13(a), the first-order natural frequency decreases gradually with the increase of temperature difference, and the contact thermal stiffness causes the first natural frequency to be larger than that not considered. It can be found that the contact thermal stiffness causes a significant change in the second order natural frequency, and the change becomes larger as the temperature increases in Fig. 13(b). The frequency difference is 8.8 Hz when the temperature difference is 200 °C. In addition, it can be found in Fig. 13(b) that the third-order eigenvalue is less sensitive to the change of contact thermal stiffness. The analysis of the dynamic characteristics of the thermal elastoplastic coupling combined rotor shows that although the natural frequencies decrease with the increase of temperature, the sensitivity of different order natural frequencies to contact thermal stiffness is different. For the combined rotor studied in this paper, the second and fourth-order natural frequencies show a more pronounced response to the change in contact thermal stiffness, with varying degrees of influence depending on the temperature difference. Therefore, the analysis of the variation of dynamic characteristics with temperature should be combined with the specific combined rotor structure.

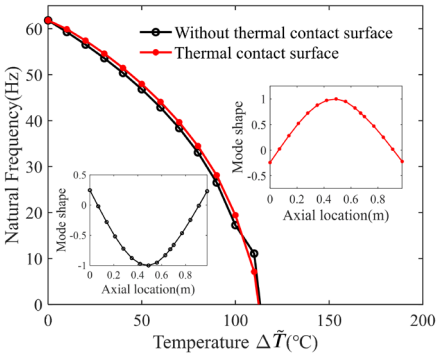

(a) The first-order natural frequency

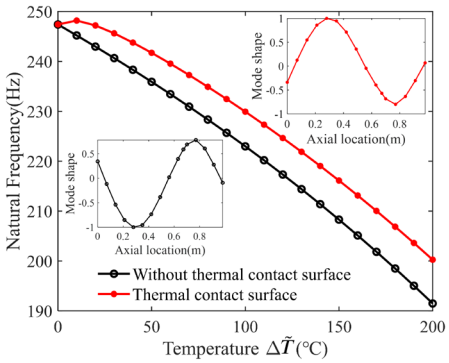

(b) The second-order natural frequency

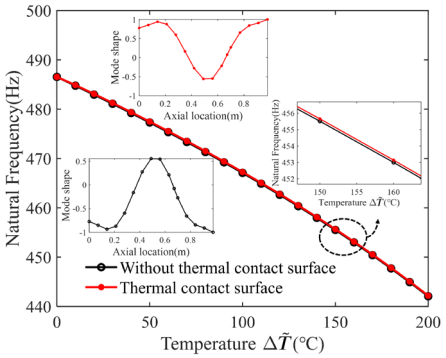

(c) The third-order natural frequency

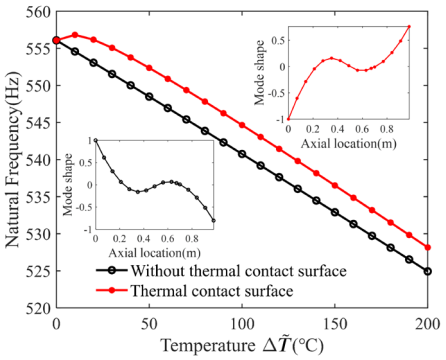

(d) The fourth-order natural frequency

Fig. 13 The first four natural frequencies with the temperature difference changes

CONCLUSIONS AND PERSPECTIVES

A thermal elastoplastic fractal surface contact stiffness model considering temperature load is presented, and its application in the combined rotor model is expanded to further improve the accuracy of the existing thermal elastoplastic coupling rotor dynamics modelling in this work. The investigation yields several valuable conclusions as follows:

(1) The normal total loads of the thermal elastoplastic coupling asperity and the bolt connection are derived using fractal theory and load distribution. The normal total stiffness of the asperity and the bolted surface are obtained. Furthermore, combined with the actual bolt distribution form and energy change, the

thermal elastoplastic coupling combined rotor dynamics model considering the contact thermal stiffness is constructed.

(2) The stiffness dominated by temperature load and preload both increase with the temperature difference, leading to an overall increase in the total normal stiffness. The reason for this change is that the actual contact area of the asperity changes under the temperature load. However, the limitation is that the coupling effect of temperature load and bolt preload is not fully considered. Preliminary analysis indicates that the preload primarily governs the initial real contact area and interfacial stiffness, whereas temperature-induced thermal expansion can alter the preload magnitude through differential thermal deformation—particularly in bolted joints. This interaction may result in complex variations in contact behavior. Therefore, understanding the coupled effects of multiple loads remains a critical direction for future research.

(3) Elevated temperature significantly reduces the eigenvalue of the combined rotor. The contact thermal stiffness also affects the eigenvalue, which depends on the sensitivity of each natural frequency of the combined rotor to the contact stiffness of the connection position. For instance, in this study, the second- and fourth-order natural frequencies of the rotor experience a considerable increase with the rise in contact thermal stiffness, while the first- and third-order natural frequencies undergo slight changes.

(4) While this study employs a linearized model to investigate the influence of thermal contact stiffness on rotor dynamics, it is important to acknowledge that nonlinear effects—particularly in contact interfaces—may become significant under elevated temperatures. These nonlinearities may arise from factors such as temperature-dependent material properties, microslip at contact surfaces, stiffness degradation, and thermally induced geometric changes. Such phenomena could lead to amplitude-dependent stiffness or localized dynamic instabilities that are not captured by linear models. In future work, incorporating nonlinear contact mechanics into the model will be considered to more accurately reflect the system's behavior under realistic thermal and mechanical loading conditions.

(5) This study examines a simplified assembled rotor featuring a single bolted interface. However, practical rotor systems typically consist of multiple components—such as shafts, disks, and blades—connected through various methods, including bolted joints, rabbets, and curvic couplings. These systems often operate under complex, high-temperature conditions, resulting in more intricate thermal contact phenomena at the interfaces. To capture this complexity, future research will apply the proposed method to more realistic rotor systems. This expansion is expected to not only improve the accuracy of thermoelastic predictions but also to develop vibration control strategies for next-generation turbine systems.

ACKNOWLEDGMENT

This work was supported by the National Natural Science Foundation of China (Grant No. 52475060), the State Key Laboratory of Mechanics and Control for Aerospace Structures (Grant No. MCAS-S-0425G02), and the Outstanding Doctoral Dissertation Funding of NUAA (Grant No. BCXJ25-13). We sincerely appreciate the valuable support provided by the editor and reviewers.

REFERENCES

Ajul, E., and Chanda, S., "Estimation of thermal contact conductance of spacecraft heat sink bolted joints," *Appl. Therm. Eng.*, Vol. 224, pp.120078 (2023).

Cheng, J., Sun, Y., Yu, Y., Chen, L., and Ma, X., "Nonlinear thermo-mechanical coupled analysis of high temperature effect on strength, contact stress and ultimate torque of tool joint." *Int. J. Pres. Ves. Pip.*, Vol. 188, pp.104221 (2020).

Han, X., Zhou, J., and Zhou, Y., "Analysis and Suppression of Self-Excited Vibration of Flexible Rotor AMBs System," *J. Vib. Eng. Technol.*, pp.1–12 (2021).

Hartwigsen, C.J., Song, Y., McFarland, D.M., Bergman, L.A., and Vakakis, A.F., "Experimental study of non-linear effects in a typical shear lap joint configuration," *J. Sound. Vib.*, Vol.277, pp.327–351 (2004).

Hou, P., and Zhang, W., "Bolt Coupling Structure of Contact Stress and the Influence Factors of Joint Stiffness Based on Finite Element Method," *Pro.Comput. Sci.*, Vol. 208, pp.658–665 (2022).

Kogut, L., and Komvopoulos, K., "Analysis of the spherical indentation cycle for elastic–perfectly plastic solids," *J. Mater. Res.* Vol. 19, pp.3641–3653 (2004).

Li, C., Jiang, Y., Qiao, R., and Miao, X., "Modeling and parameters identification of the connection interface of bolted joints based on an improved micro-slip model," *Mech. Syst. Signal. Pr*, Vol.153, pp.107514 (2021).

Li, D., Botto, D., Xu, C., Liu, T., and Gola, M., "A micro-slip friction modeling approach and its application in underplatform damper kinematics," *Int. J. Mech. Sci.*, Vol.161–162, pp.105029 (2019).

Liu, J., Ma, C., Wang, S., Wang, S., and Yang, B., "Contact stiffness of spindle-tool holder based on fractal theory and multi-scale contact mechanics model," *Mech. Syst. Signal. Pr.*, Vol.119, pp.363–379 (2019a).

Liu, J., Ma, C., Wang, S., Wang, S., and Yang, B.,

"Thermal contact resistance between bearing inner ring and shaft journal," *Int. J. Therm. Sci*., Vol.138, pp.521–535 (2019b).

Magyar, B., and Sauer, B., "Methods for the simulation of the pressure, stress, and temperature distribution in the contact of fractal generated rough surfaces," *P. I. Mech. Eng. J.-J. Eng.*, Vol.231, pp.489–502 (2017).

Majumdar, A., and Tien, C.L., "Fractal Network Model for Contact Conductance," *J. Heat. Trans.*, Vol.113, No.3, pp.114–133 (1991).

Peng, H., Liu, Z., Huang, F., and Ma, R., "A study of elastic–plastic contact of statistical rough surfaces," P. I. Mech. Eng. J.-J. Eng. Vol.227, pp.1076–1089 (2013).

Peng, H., Zhou, Z., Feng, J., Yu, X., and Liu, Z., "Prediction of the thermal bow of rotor based on the measured displacement and temperature," *Int. J. Distrib. Sens. N.*, Vol.16, pp.155014772096299 (2020).

Ping, V., Cunjian, Z., Wei, Z., Qingkai, H., and Wei, S., "Stiffness of bolted joint and dynamic characteristics of rotors under non-parallel contact," *J. Econ. Dyn. Control.*, Vol.16, No.6, pp.561-567 (2018).

Shamoto, E., Hashimoto, Y., Shinagawa, M., and Sencer, B., "Analytical prediction of contact stiffness and friction damping in bolted connection," *Cirp. Ann.* Vol.63, pp.353–356 (2014).

Shi, W., and Zhang, Z., "Contact characteristic parameters modeling for the assembled structure with bolted joints," *Tribol. Int.* Vol.165, pp.107272 (2022).

Shlykov, Y., and Ganin, Y., "Thermal resistance of metallic contacts," *Int. J. Heat. Mass. Tran.* Vol.7, pp. 921-929 (1964).

Si, Z., Li, Y., Wen, L., and Du, X., "Simulation and Analysis of the Temperature Field and the Thermal Stress of an Inverted-Siphon Concrete Structure Based on the Contact Friction Element," *Ksce. J. Civ. Eng.* Vol.24, pp.2449–2457 (2020).

Sun, X., and Xing, W., "Fractal model of thermal contact conductance of rough surfaces based on elliptical asperity," *Ind. Lubr. Tribol.* Vol.75, pp.424–431 (2023).

Tian, H., "Normal Contact Mechanics Model of Fixed Joint Interface Adopting Anisotropic Fractal Geometrical Theory," *J. Mech. Eng.* Vol.49, pp.108 (2013).

Tirovic, M., and Voller, G.P., "Interface pressure distributions and thermal contact resistance of a bolted joint," *Proc. R. Soc. A*. Vol.461, pp.2339–2354 (2005).

Xiao, W.W., Mao K.M., Li B., and Lei S., "Contact stiffness of bolted joint with different material combination in machine tools," *J. Vibroeng.* Vol.16, pp.3281–3293 (2014).

Yan, W., and Komvopoulos, K., "Contact analysis of elastic-plastic fractal surfaces," *J. Appl. Phys.* Vol.84, pp.3617–3624 (1998).

Yin, Y., Cai, L., Liu, Z., Zhao, Y., and Cheng, Q., "Normal Stiffness model of bolted joint based on the modified three-dimensional elastic-plastic contact fractal model," *IOP Conf. Ser.: Mater. Sci. Eng.* Vol.382, pp.032042 (2018).

Yuan, S.X., Zhang, Y.Y., Zhang, Y.C., and Jiang, X.J., "Stress distribution and contact status analysis of a bolted rotor with curvic couplings ARCHIVE," *P. I. Mech. Eng. C.-J. Mec.* Vol.203-210, No.1, pp.1–15 (2010).

Zhao, G., Xiong, Z., Jin, X., Hou, L., and Gao, W., "Prediction of contact stiffness in bolted interface with natural frequency experiment and FE analysis," *Tribol. Int*. Vol.127, pp.157–164 (2018).

Zhou, H., Long, X., Meng, G., and Liu, X., "A Stiffness Model for Bolted Joints Considering Asperity Interactions of Rough Surface Contact," *J. Tribol.* Vol.144, pp.011501 (2022).

Zhou, Y., Xu, Y., Zhou, J., and Mahfoud, J., "Numerical and experimental investigations on the dynamic behavior of a rotor-AMBs system considering shrink-fit assembly," *Mech. Syst. Signal. Pr.* Vol.224, pp.111980 (2025).

Ziaei-Rad, S., Kouchaki, E., and Imregun, M., "Thermoelastic Modeling of Rotor Response With Shaft Rub," *Int. J. Pres. Ves. Pip.* Vol.77, pp.061010 (2010).

NOMENCLATURE

T_a, T_b	Temperatures of the contact surface-a/b
E_a, E_b	Elastic modulus of the contact surface-a/b
μ_a, μ_b	Poisson's ratio of the contact surface-a/b
R_a, R_b	Asperity radius
H_a, H_b	Material hardness
α_a, α_b	Thermal expansion coefficient
Y_a, Y_b	Yield strength
$\tilde{T}$	Equivalent temperature
$\tilde{E}$	Equivalent elastic modulus
$\tilde{R}$	Equivalent asperity radius
$\tilde{H}$	Equivalent material hardness
$\tilde{\alpha}$	Equivalent thermal expansion coefficient
$\tilde{Y}$	Equivalent yield strength
$L, 1/L$	Sample length, sampling frequency
D_f	Fractal dimension
G_f	Fractal roughness
γ	Frequency density of fractal profile
$\phi_{m,n}$	Random phase
L_s	Truncation length
n	Upper limit of the frequency index
m_0	Dimension of the rough surface

r_t Truncation radius
n_t Frequency index
χ Deformation of the asperity in the z direction
ε The normal strain
f_e, f_p Total normal loads of the asperity in the elastic and plastic deformation regions
a_r Real contact area
a_t Truncated contact area
a_{t_c} Critical truncation area
a_{t_max} Maximum truncation area of the asperity
φ Domain expansion factor
A_t Total truncated contact area
A_r Total actual contact area
A_a Nominal contact area
F_T, F_M Temperature load and preload
k_n Asperity stiffness
K_n, K_{n_M}, K_{n_T} Total, mechanical and temperature normal contact stiffness
k_f, k_q Normal stiffness, tangential stiffness
r Radius of the contact surface
N Number of bolts
β Proportional coefficient
M, C, G, K Mass, damping, gyroscopic, stiffness matrices
K_T Temperature load dominated stiffness
K_c Additional contact stiffness matrix
K_{spring} Bearing support stiffness matrix
$f(t), M(t)$ Unbalanced force and bending moment
F_T, F_M Temperature load and preload
M_b, F_b Preload moment, bolt preload force
q Generalized coordinates
$\overline{p_T}$ Average thermal pressure
α Diameter factor
$\Delta\tilde{T}$ Temperature difference
Ω Rotor speed